Journal of Thermal Analysis and Calorimetry (2020) 139:3345–3360
https://doi.org/10.1007/s10973-019-08672-0

# Influence of radiative heat transfer on the thermal characteristics of nanofluid flow over an inclined step in the presence of an axial magnetic field

M. Atashafrooz[1]

Received: 29 May 2019 / Accepted: 6 August 2019 / Published online: 14 August 2019


## Abstract

This research analyzes the influences of radiation heat transfer and Brownian movement on the thermal characteristics of nanofluid flow over an inclined step in the presence of an axial magnetic field. The Rosseland approximation is applied to simulate the divergence of radiative heat flux in the energy equation. The $Al_2O_3$–$H_2O$ and CuO–$H_2O$ nanofluids are considered as the working fluid. The KKL correlation is used for modeling the Brownian movement influence on the effective viscosity and thermal conductivity. The impacts of radiation parameter $(0 \le Rd \le 1)$, nanoparticles concentration $(0 \le \phi \le 0.04)$ and Lorentz force $(0 \le Ha \le 60)$ on temperature fields, mean bulk temperature and convective, radiative and total Nusselt numbers are examined with full details. The results show that the impact of CuO nanoparticles on the average of total heat transfer rates is greater that the influence of $Al_2O_3$ nanoparticles on them. Besides, the highest values of total heat transfer rates occur in the absence of magnetic field and for the highest values of $Rd$ and $\phi$ parameters.

**Keywords** Thermal radiation · Lorentz force · MHD flow · Nanofluid · Brownian movement · BFS

## List of symbols

| | |
|---|---|
| $B_0$ | Magnetic field strength |
| $C_p$ | Specific heat (J kg$^{-1}$ K$^{-1}$) |
| $h$ | Channel height upstream of BFS, (m) |
| $H$ | Channel height downstream of BFS, (m) |
| $Ha$ | Hartmann number |
| $\overrightarrow{F_l}$ | Lorentz force |
| $k$ | Thermal conductivity, (W m$^{-1}$ K$^{-1}$) |
| $L_D$ | Channel length downstream of BFS, (m) |
| $L_r$ | Reattachment length, (m) |
| $L_U$ | Channel length upstream of BFS, (m) |
| $Nu$ | Nusselt number |
| $p$ | Pressure, (N m$^{-2}$) |
| $P$ | Dimensionless pressure |
| $Pr$ | Prandtl number |
| $\vec{q}$ | Heat flux |
| $Re$ | Reynolds number |
| $Rd$ | Radiation parameter |
| $T$ | Temperature, (K) |
| $(u, v)$ | $x$- and $y$-components of velocity, (m s$^{-1}$) |
| $(U, V)$ | Dimensionless $X$- and $Y$-component of velocity |
| $\vec{V}$ | Velocity vector |

## Greek symbols

| | |
|---|---|
| $\phi$ | Nanoparticles concentration |
| $\mu$ | Dynamic viscosity, (N s m$^{-2}$) |
| $\rho$ | Density, (kg m$^{-3}$) |
| $\sigma$ | Electrical conductivity |
| $\Theta$ | Dimensionless temperature |

## Subscripts

| | |
|---|---|
| c | Convective |
| f | Fluid |
| in | Inlet section |
| nf | Nanofluid |
| r | Radiative |
| s | Solid nanoparticles |
| t | Total |

✉ M. Atashafrooz
m.atashafrooz@sirjantech.ac.ir;
Meysam.atashafrooz@yahoo.com

[1] Department of Mechanical Engineering, Sirjan University of Technology, Sirjan, Iran

## Introduction

Analysis of magnetohydrodynamics (MHD) nanofluid flows is one of the important and noteworthy issues in heat transfer sciences. This subject has so far been studied by

many scholars under different conditions [1–11]. This attention is due to the important role of this type of flow in the control of hydrothermal behaviors. In fact, in this type of flow, the heat transfer rates can be controlled by adding solid nanoparticles to the base fluid (nanofluid) and applying a magnetic field in the flow domain (MHD flow). There are many researches about the separate role of nanofluid [12–26] and magnetic field [27–33] on heat transfer features of fluid flow. Some of these researches have been dedicated to study the role of thermal radiation on the improvement of convection heat transfer rates [34–40]. Among these articles, Ghalambaz et al. [41] and Sheikholeslami et al. [42] analyzed the influences of thermal radiation and viscous dissipation on convection heat transfer of nanofluid flow in a square cavity under different conditions. Safaei et al. [43] simulated the coupling between thermal radiation and free convection heat transfer of nanofluid flow in a shallow cavity using the lattice Boltzmann method. Interacting effects of magnetic field and thermal radiation on hydrothermal behaviors of $Al_2O_3$–$H_2O$ nanofluid inside a permeable media were simulated by Sheikholeslami et al. [44]. They reported that the convection enhances as the radiation parameter increases, but it reduces by increasing the magnitudes of Hartmann number. In another research, Sheikholeslami and Rokni [45] numerically investigated the role of thermal radiation on heat transfer rates of $Fe_2O_3$–ethylene glycol nanofluid flow inside a porous enclosure considering the influences of an external electric field. It can be concluded that average Nusselt number enhances as Darcy number and radiation parameter increase. Besides, from a different point of view, the impact of radiative heat transfer on thermal behaviors of engineering problems was simulated using the discontinuous finite element method [46, 47].

The geometry of equipment used in industries and engineering applications is also one of the important factors in controlling the hydrothermal behaviors [48–50]. The channels with step are one of the most important geometries that are used in industries and engineering equipment. Therefore, analysis of fluid flow in these geometries is another important subject in thermal sciences. These kinds of flows are considered as a benchmark problem and have an essential role in controlling the heat transfer patterns. The hydrothermal patterns of these flows were extensively investigated in the absence of nanoparticles and magnetic field influences [51–58]. In these studies, the effects of different parameters such as baffles, obstacles, radiative heat transfer and Reynolds number on the flow and thermal characteristics were analyzed. Of course, given the industrial application of these flows, many scholars studied the impacts of solid nanoparticles on the hydrothermal features of step flows [59–64]. Among these articles, Mohammad et al. [65] and Alawi et al. [66] summarized and reviewed a large numbers of previous researches about the heat transfer characteristics of various nanofluid flows in channels having the steps. Selimefendigil and Oztop [67] numerically investigated the influences of different shaped obstacles on heat transfer rates of Cu–$H_2O$ nanofluid over a step with a corrugated bottom wall. They reported that the obstacle shapes and Reynolds number have notable impacts on the magnitudes of average Nusselt number. In other articles, two experimental and numerical studies were performed by Kherbeet et al. [68, 69] to investigate influences of various parameters on hydrothermal characteristics of nanofluid flow in the channels having the backward (BFS) and forward (FFS) facing steps. In another recent study, Atashafrooz [70] numerically simulated the impact of Ag nanoparticles on hydrothermal behaviors of fluid flow in a 3-D channel with an inclined BFS.

It should be noted that the impacts of magnetic field on heat transfer features of step flow have been less studied compared to the nanofluids influences. Among these studies, Abbasi and Nassrallah [71] numerically analyzed the role of Lorentz force on the hydrothermal characteristics of step flow. They found that velocity field and Nusselt number distributions are dependent on the Stuart number. In other researches, Selimefendigil and Oztop [72] and Atashafrooz et al. [73, 74] examined the impacts of different parameters on thermal patterns and entropy generation of MHD nanofluid flow in channels with step. They presented that the Hartmann number, buoyancy force, inclination angle of magnetic field and concentration of solid nanoparticles affected the flow irreversibility and heat transfer rates.

Although so far several researches have been done to analyze the hydrothermal behaviors in ducts with step, but as it is clear from the literature review, the effects of thermal radiation on forced convection heat transfer of MHD nanofluid flow in a duct with an inclined BFS are still not analyzed and simulated. This motivates the current research, such that the interacting impacts of radiative heat transfer, nanoparticles concentration, Brownian movement and magnetic field strength on the thermal features of MHD nanofluid flow over an inclined BFS are investigated here for the first time with full details.

## Problem definition

The geometry and physical configuration of regarded problem for present research is depicted in Fig. 1. The relevant details and boundary conditions of considered geometry are obviously seen from this figure. This geometry includes a horizontal channel with an inclined BFS ($\beta = 60^\circ$). The $Al_2O_3$–$H_2O$ and CuO–$H_2O$ nanofluids are selected as the working fluid. Thermophysical

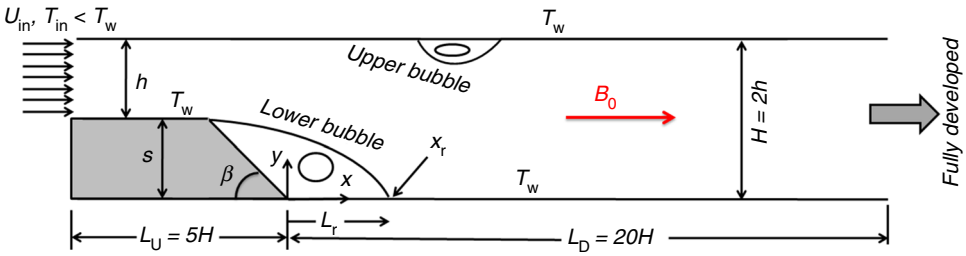


**Fig. 1** Geometry and physical configuration of problem

**Table 1** Thermophysical characteristics of $H_2O$ and nanoparticles of CuO and $Al_2O_3$ [73, 74]

| Property | $\rho$/kg m$^{-3}$ | $C_p$/J kg$^{-1}$ K$^{-1}$ | $k$/W m$^{-1}$ K$^{-1}$ | $\mu$/kg m$^{-1}$ s$^{-1}$ | $\sigma$/1 Ω$^{-1}$ m$^{-1}$ | $d_s$/nm |
|---|---|---|---|---|---|---|
| $H_2O$ | 997.1 | 4179 | 0.613 | 0.001003 | 0.05 | – |
| CuO | 6500 | 540 | 18 | – | $10^{-10}$ | 29 |
| $Al_2O_3$ | 3970 | 765 | 25 | – | $10^{-12}$ | 47 |

characteristics of $H_2O$ and nanoparticles of CuO and $Al_2O_3$ are presented and tabulated in Table 1. Also, it is considered that an axial magnetic field with uniform strength of $B_0$ affects the whole domain of nanofluid flow.

## Governing equations

The vector forms of the basic equations for the current study can be written as follows:

$$\nabla \cdot \vec{V} = 0 \tag{1}$$

$$\vec{V} \cdot \nabla \vec{V} = -\frac{1}{\rho_{nf}} \nabla p + \frac{\mu_{nf}}{\rho_{nf}} \left(\nabla^2 \vec{V}\right) + \frac{1}{\rho_{nf}} \overrightarrow{F_l} \tag{2}$$

$$\vec{V} \cdot \nabla T = \frac{k_{nf}}{\rho_{nf} C_{p_{nf}}} \left(\nabla^2 T\right) - \frac{1}{\rho_{nf} C_{p_{nf}}} \nabla \cdot \overrightarrow{q_r} \tag{3}$$

The terms of $\overrightarrow{F_l}$ and $\nabla \cdot \overrightarrow{q_r}$ are the Lorentz force and divergence of radiative heat flux, respectively. These two terms with the effective characteristics of nanofluid would be computed in the following sections.

### Computation of effective characteristics of nanofluid

To evaluate the effective viscosity $(\mu_{nf})$, density $(\rho_{nf})$, thermal conductivity $(k_{nf})$ and specific heat $\left(C_{p_{nf}}\right)$ of nanofluid, the following relationships are applied [75, 76]:

$$\mu_{nf} = \frac{\mu_f}{(1-\phi)^{2.5}} + \frac{k_{Brownain}}{k_f} \times \frac{\mu_f}{Pr} \tag{4}$$

$$\rho_{nf} = \phi \rho_s + (1-\phi)\rho_f \tag{5}$$

$$k_{nf} = k_f \left( 1 + \frac{3\left(\frac{k_s}{k_f} - 1\right)\phi}{\left(\frac{k_s}{k_f} + 2\right) - \left(\frac{k_s}{k_f} - 1\right)\phi} \right) + k_{Brownain} \tag{6}$$

$$(\rho C_p)_{nf} = \phi(\rho C_p)_s + (1-\phi)(\rho C_p)_f \tag{7}$$

According to Eqs. (4) and (6), impact of Brownian movement on the parameters of $\mu_{nf}$ and $k_{nf}$ is considered. To obtain the term of $k_{Brownain}$, the KKL correlation is applied as follows [44, 75, 76]:

$$k_{Brownain} = 5 \times 10^4 \times \left(\phi \times \rho_f \times C_{p_f}\right) \times \sqrt{\frac{C_b T}{\rho_s d_s}} \times G(T, \phi, d_s) \tag{8}$$

In this equation [44, 75, 76]:

$$\begin{aligned} G(T, \phi, d_s) =& (M_1 + M_2 \mathrm{Ln}(d_s) + M_3 \mathrm{Ln}(\phi) \\ &+ M_4 \mathrm{Ln}(d_s)\mathrm{Ln}(\phi) + M_5 \mathrm{Ln}(d_s)^2)\mathrm{Ln}(T) \\ &+ M_6 + M_7 \mathrm{Ln}(d_s) + M_8 \mathrm{Ln}(\phi) \\ &+ M_9 \mathrm{Ln}(d_s)\mathrm{Ln}(\phi) + M_{10} \mathrm{Ln}(d_s)^2 \end{aligned} \tag{9}$$

The coefficients of $M_i (i = 1, 2, \ldots, 10)$ are dependent on the type of nanofluid. The values of these coefficients for CuO–$H_2O$ and $Al_2O_3$–$H_2O$ nanofluids are presented in Table 2. Besides, the subscripts of $f$ and $s$ in Eqs. (4)–(9)

**Table 2** The coefficients values of CuO–$H_2O$ and $Al_2O_3$–$H_2O$ nanofluids in Eq. (9) [73, 74]

| $M_i$ | CuO–$H_2O$ | $Al_2O_3$–$H_2O$ |
|---|---|---|
| $M_1$ | − 26.593310846 | 52.813488759 |
| $M_2$ | − 0.403818333 | 6.115637295 |
| $M_3$ | − 33.3516805 | 0.6955745084 |
| $M_4$ | − 1.915825591 | $4.17455552786 \times 10^{-2}$ |
| $M_5$ | $6.42185846658 \times 10^{-2}$ | 0.176919300241 |
| $M_6$ | 48.40336955 | − 298.19819084 |
| $M_7$ | − 9.787756683 | − 34.532716906 |
| $M_8$ | 190.245610009 | − 3.9225289283 |
| $M_9$ | 10.9285386565 | − 0.2354329626 |
| $M_{10}$ | − 0.72009983664 | − 0.999063481 |

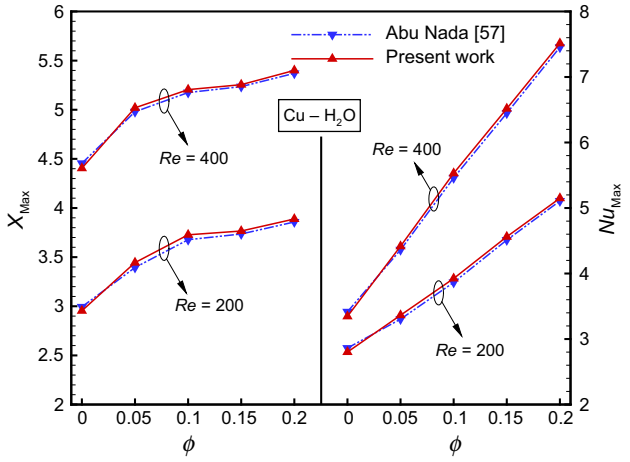


**Fig. 2** Comparison of $X_{\mathrm{Max}}$ and $Nu_{\mathrm{Max}}$ magnitudes at various magnitudes of $\phi$ with the findings of Abu-Nada [57]

denote, respectively, the thermophysical characteristics of base fluid ($H_2O$) and solid nanoparticles (CuO, $Al_2O_3$), where the $\phi$ symbol is the concentration of nanoparticles. Also, the $C_b$ parameter in Eq. (8) is the Boltzmann constant $\left(C_b \approx 1.38 \times 10^{-23}\,\mathrm{J\,K^{-1}}\right)$.

## Computation of Lorentz force

The Lorentz force appears in the momentum equations due to the existence of magnetic field. According to the Ohm's low, this force can be obtained as follows [33]:

$$\overrightarrow{F_l} = \sigma_{nf}\left(\vec{E} + \left(\vec{V} \times \vec{B}\right)\right) \times \vec{B} \tag{10}$$

In the absence of electric field $\left(\vec{E} = 0\right)$, the $\overrightarrow{F_l}$ are computed as [33]:

$$\overrightarrow{F_l} = \sigma_{nf}\left(\vec{V} \times \vec{B}\right) \times \vec{B} \tag{11}$$

The term of $\sigma_{nf}$ in the above equation is the effective electrical conductivity of nanofluid that can be computed as [75, 76]:

**Table 4** Influence of CuO and $Al_2O_3$ nanoparticles on the magnitudes of average total Nusselt number $\left(\overline{Nu}_t\right)$ at various values of $Rd$ parameter $(Ha = 20, \phi = 0.04)$

| $Rd$ | $Al_2O_3$–$H_2O$ | CuO–$H_2O$ |
|---|---|---|
| 0 | 4.986771 | 5.161620 |
| 0.25 | 5.706675 | 5.897706 |
| 0.5 | 6.399273 | 6.651880 |
| 0.75 | 7.189846 | 7.435231 |
| 1 | 7.972395 | 8.254035 |

$$\sigma_{nf} = \sigma_f\left(1 + \frac{3\left(\frac{\sigma_s}{\sigma_f} - 1\right)\phi}{\left(\frac{\sigma_s}{\sigma_f} + 2\right) - \left(\frac{\sigma_s}{\sigma_f} - 1\right)\phi}\right) \tag{12}$$

Also, $\vec{B} = B_0\vec{i}$ and $\vec{V} = u\vec{i} + v\vec{j}$.

By substituting Eq. (12) and parameters of $\vec{B}$ and $\vec{V}$ in Eq. (11), the Lorentz force is obtained as follows:

$$\overrightarrow{F_l} = -\left(\sigma_f\left(1 + \frac{3\left(\frac{\sigma_s}{\sigma_f} - 1\right)\phi}{\left(\frac{\sigma_s}{\sigma_f} + 2\right) - \left(\frac{\sigma_s}{\sigma_f} - 1\right)\phi}\right) \times v \times B_0^2\right)\vec{j} \tag{13}$$

## Computation of radiative heat flux

Since, the working fluid in this study is MHD nanofluid, the radiative heat flux can be obtained using Rosseland approximation as [41]:

$$\overrightarrow{q_r} = q_{r_x}\vec{i} + q_{r_y}\vec{j} \tag{14}$$

and

$$q_{r_x} = \frac{-4\sigma^*}{3\beta_R}\frac{\partial T^4}{\partial x} \tag{15}$$

$$q_{r_y} = \frac{-4\sigma^*}{3\beta_R}\frac{\partial T^4}{\partial y} \tag{16}$$

**Table 3** Comparison of $\overline{Nu}$ and $\theta_{\mathrm{Max}}$ magnitudes at different values of $Ha$ with the results of Ref. [79] $(\phi = 0.02, Re = 100)$

| $Ha$ | $\theta_{\mathrm{Max}}$ | | | $\overline{Nu}$ | | |
|---|---|---|---|---|---|---|
| | Present solution | Ref. [79] | Difference*(%) | Present solution | Ref. [79] | Difference*(%) |
| 0 | 0.353 | 0.349 | 1.146 | 4.465 | 4.394 | 1.615 |
| 10 | 0.322 | 0.327 | 1.529 | 4.983 | 5.020 | 0.737 |
| 20 | 0.307 | 0.311 | 1.286 | 5.512 | 5.573 | 1.094 |
| 30 | 0.298 | 0.303 | 1.650 | 5.827 | 5.903 | 1.287 |
| 40 | 0.295 | 0.299 | 1.337 | 6.049 | 6.117 | 1.110 |

$$\text{Difference}^*(\%) = \left|\frac{(\text{Result})_{\text{Present}} - (\text{Result})_{\text{Ref.[79]}}}{(\text{Result})_{\text{Ref.[79]}}}\right| \times 100$$

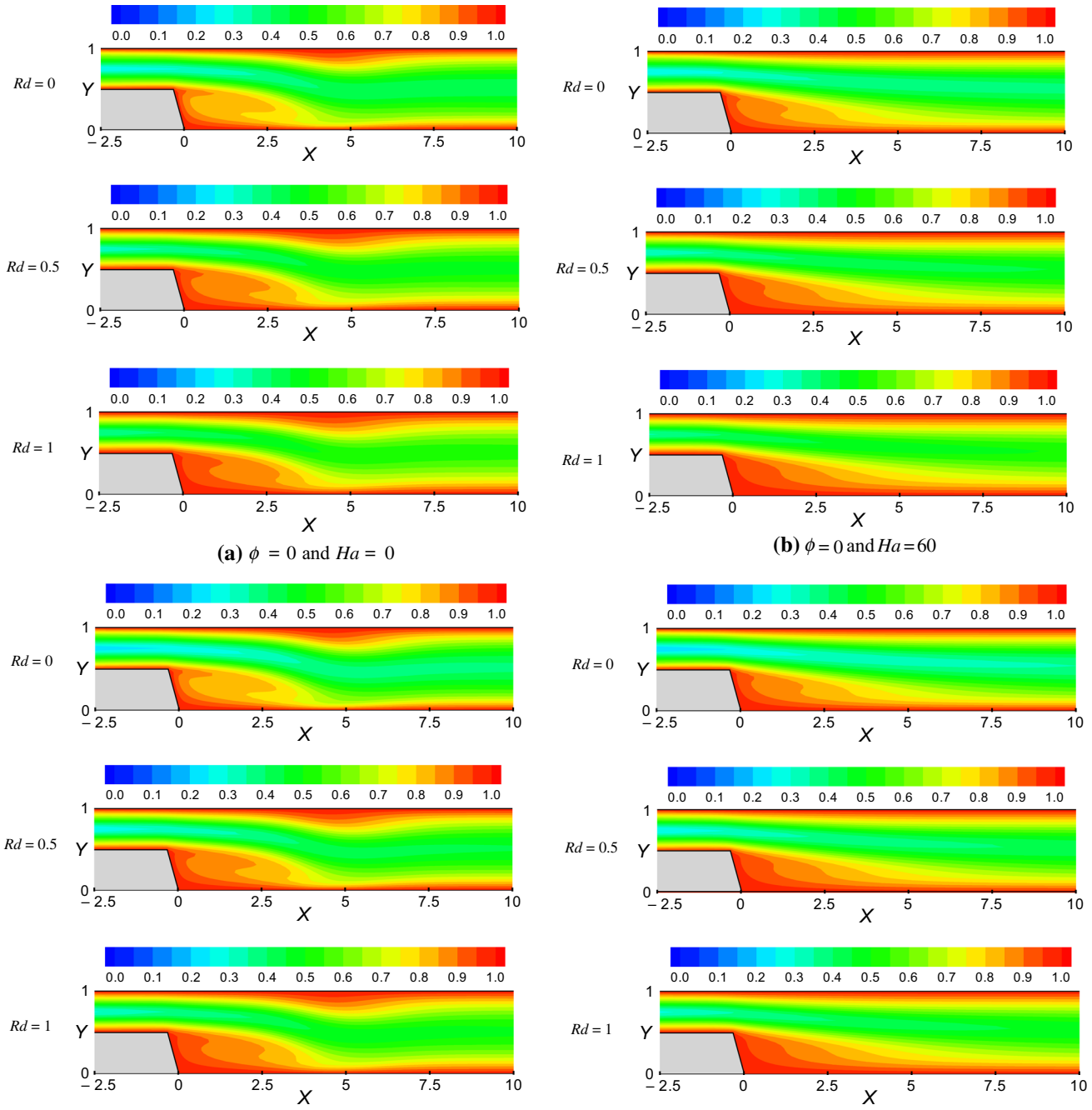


**Fig. 3** Distributions of isotherms in the duct at various magnitudes of $Rd, \phi$ and $Ha$ parameters

where $\sigma^*$ and $\beta_R$ are, respectively, the Stefan–Boltzmann constant $\left(5.67 \times 10^{-8}\,\mathrm{W\,m^{-2}\,K^{-4}}\right)$ and the coefficient of mean absorption. In Eqs. (15) and (16), the $T^4$ can be approximated using Taylor series as follows [39, 41, 45]:

$$T^4 = 4(T_{in})^3 T - 3(T_{in})^4 \tag{17}$$

Therefore, the divergence of radiative heat flux for MHD nanofluid flow would be calculated using the below equation [39, 41, 45]:

$$\nabla \cdot \overrightarrow{q_r} = \frac{-16(T_{in})^3 \sigma^*}{3\beta_R}\left(\frac{\partial^2 T}{\partial x^2} + \frac{\partial^2 T}{\partial y^2}\right) \tag{18}$$

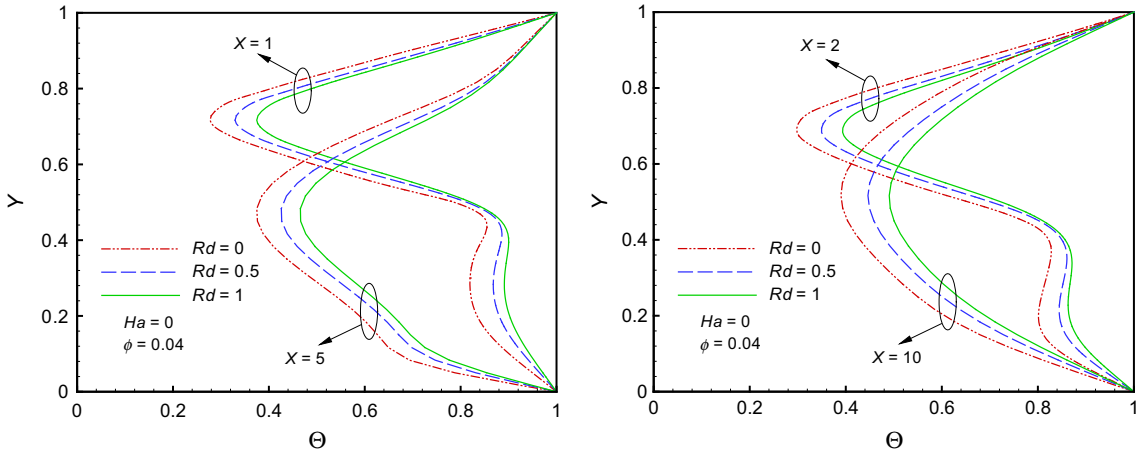


**(a)** $Ha = 0$ and $\phi = 0.04$

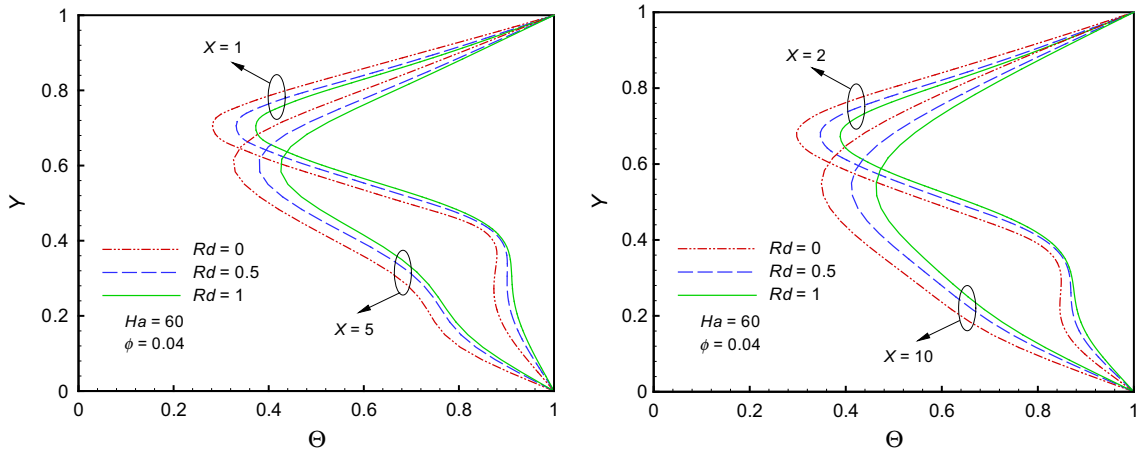


**(b)** $Ha = 60$ and $\phi = 0.04$

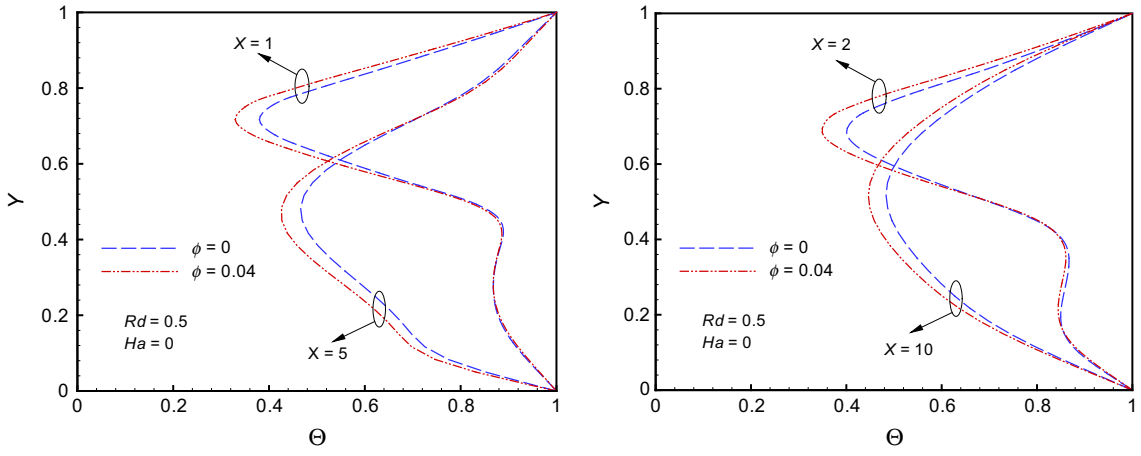


**(c)** $Rd = 0.5$ and $Ha = 0$

**Fig. 4** Temperature variations along $Y$ axis at various magnitudes of $Rd$, $\phi$ and $Ha$ parameters

## Dimensionless forms of governing equations and boundary conditions

By substituting Eqs. (13) and (18) into momentum and energy equations and using the dimensionless terms, the non-dimensional forms of governing equations can be rewritten as:

$$\frac{\partial U}{\partial X} + \frac{\partial V}{\partial Y} = 0 \tag{19}$$

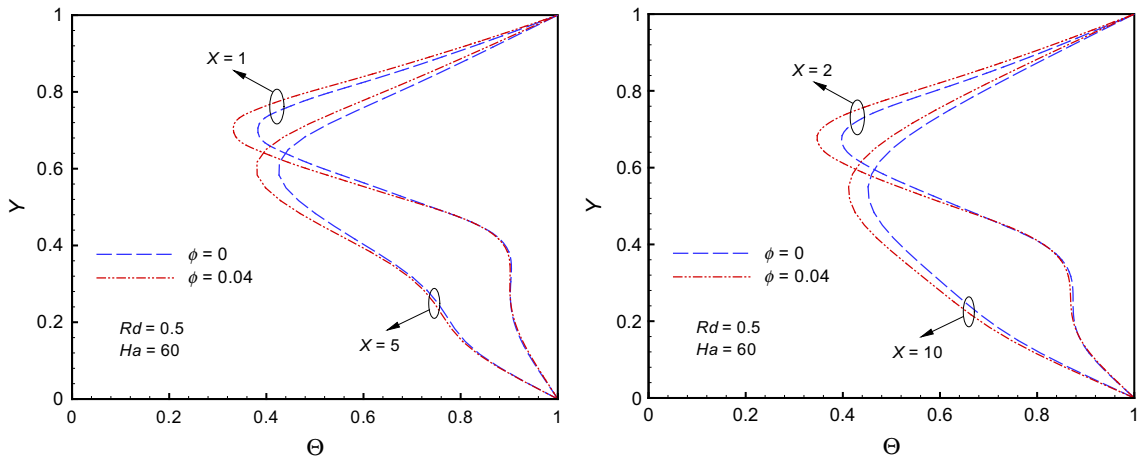


**(d)** $Rd = 0.5$ and $Ha = 60$

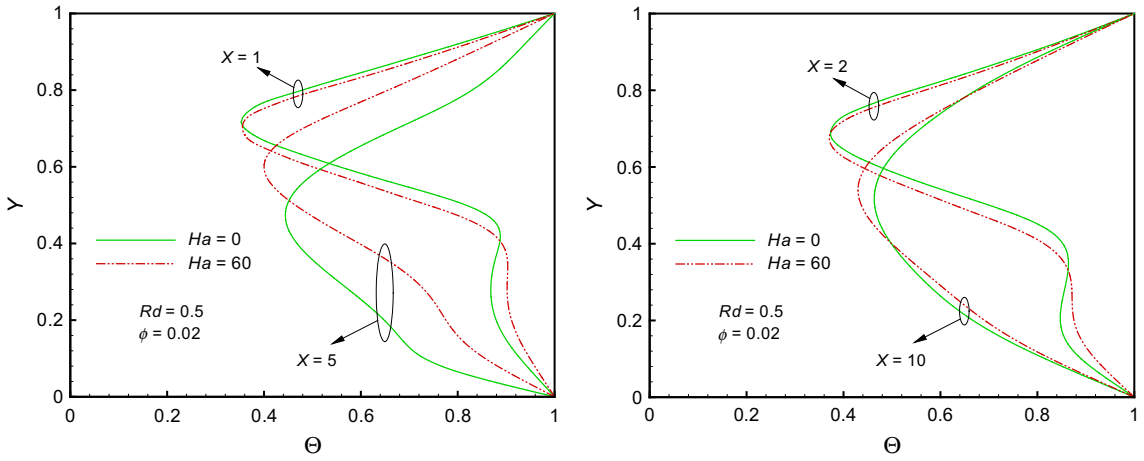


**(e)** $Rd = 0.5$ and $\phi = 0.02$

**Fig. 4** continued

$$U\frac{\partial U}{\partial X}+V\frac{\partial U}{\partial Y}=\left(\frac{-1}{(1-\phi)+\phi\frac{\rho_s}{\rho_f}}\right)\frac{\partial P}{\partial X}+\frac{1}{Re}\left(\frac{\frac{1}{(1-\phi)^{2.5}}+\frac{k_{\text{Brownain}}}{k_f\times Pr}}{(1-\phi)+\phi\frac{\rho_s}{\rho_f}}\right)\left(\frac{\partial^2 U}{\partial X^2}+\frac{\partial^2 U}{\partial Y^2}\right) \tag{20}$$

$$U\frac{\partial V}{\partial X}+V\frac{\partial V}{\partial Y}=\left(\frac{-1}{(1-\phi)+\phi\frac{\rho_s}{\rho_f}}\right)\frac{\partial P}{\partial Y}+\frac{1}{Re}\left(\frac{\frac{1}{(1-\phi)^{2.5}}+\frac{k_{\text{Brownain}}}{k_f\times Pr}}{(1-\phi)+\phi\frac{\rho_s}{\rho_f}}\right)\left(\frac{\partial^2 V}{\partial X^2}+\frac{\partial^2 V}{\partial Y^2}\right)-\left(\frac{1+\frac{3\left(\frac{\sigma_s}{\sigma_f}-1\right)\phi}{\left(\frac{\sigma_s}{\sigma_f}+2\right)-\left(\frac{\sigma_s}{\sigma_f}-1\right)\phi}}{(1-\phi)+\phi\frac{\rho_s}{\rho_f}}\right)\frac{Ha^2V}{Re} \tag{21}$$

$$U\frac{\partial\Theta}{\partial X}+V\frac{\partial\Theta}{\partial Y}=\frac{1}{RePr}\left(\frac{\left(1+\frac{3\left(\frac{k_s}{k_f}-1\right)\phi}{\left(\frac{k_s}{k_f}+2\right)-\left(\frac{k_s}{k_f}-1\right)\phi}\right)+\frac{k_{\text{Brownain}}}{k_f}}{(1-\phi)+\phi\frac{(\rho c_p)_s}{(\rho c_p)_f}}\right)\times\left(1+\frac{4}{3}Rd\left(\left(1+\frac{3\left(\frac{k_s}{k_f}-1\right)\phi}{\left(\frac{k_s}{k_f}+2\right)-\left(\frac{k_s}{k_f}-1\right)\phi}\right)+\frac{k_{\text{Brownain}}}{k_f}\right)^{-1}\right)\times\left(\frac{\partial^2\Theta}{\partial X^2}+\frac{\partial^2\Theta}{\partial Y^2}\right) \tag{22}$$

where

$$(X,Y)=\left(\frac{x}{H},\frac{y}{H}\right)\quad(U,V)=\left(\frac{u}{U_{in}},\frac{v}{U_{in}}\right)\quad P=\frac{p}{U_{in}^2}\quad Pr=\frac{\mu_f C_{p_f}}{k_f}$$
$$Ha=B_0H\sqrt{\frac{\sigma_f}{\mu_f}}\quad Re=\frac{\rho_f U_{in}H}{\mu_f}\quad\Theta=\frac{T-T_{in}}{T_w-T_{in}}\quad Rd=\frac{4(T_{in})^3\sigma^*}{k_f\beta_R} \tag{23}$$

Besides, the non-dimensional forms of the boundary conditions can be presented as:

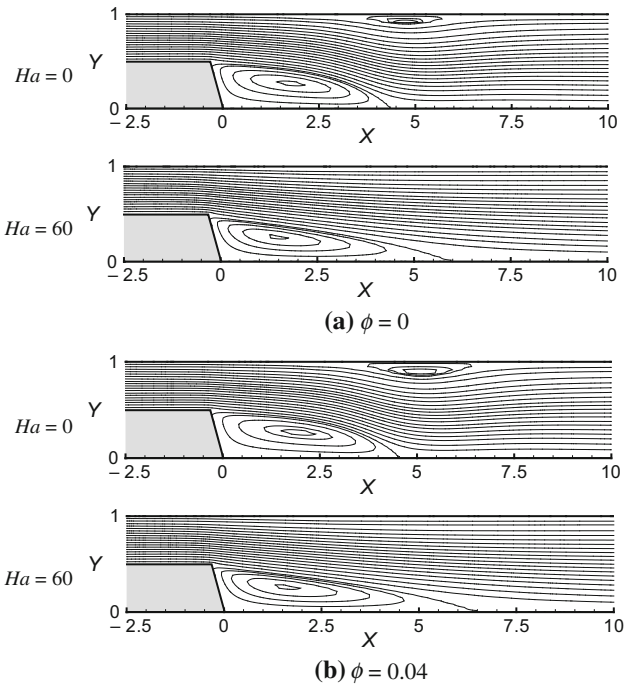


**Fig. 5** Impacts of the $\phi$ and $Ha$ parameters on the streamlines distributions in the duct

| | |
|---|---|
| At the inlet section of channel: | $U = 1,\ V = 0$ and $\Theta = 0$ |
| At all channel walls: | $U = V = 0$ and $\Theta = 1$ |
| At the outlet section of channel: | $\frac{\partial U}{\partial X} = \frac{\partial V}{\partial X} = 0$ and $\frac{\partial \Theta}{\partial X} = 0$ |

## Definition of Nusselt numbers

In convection heat transfer of MHD nanofluid flow in the presence of thermal radiation, the total heat flux $\left(\overrightarrow{q_t}\right)$ on the surfaces is obtained by summing the convective $\left(\overrightarrow{q_c}\right)$ and radiative $\left(\overrightarrow{q_r}\right)$ heat fluxes. Therefore, the total Nusselt number $(Nu_t)$ is the sum of the convective $(Nu_c)$ and radiative $(Nu_r)$ Nusselt numbers [39, 45]. These Nusselt numbers are computed along the bottom wall of channel and downstream of the BFS $\left(0 \le X \le \frac{L_D}{H} \text{ and } Y = 0\right)$ as:

$$Nu_c(X) = -\left(1 + \frac{3\left(\frac{k_s}{k_f} - 1\right)\phi}{\left(\frac{k_s}{k_f} + 2\right) - \left(\frac{k_s}{k_f} - 1\right)\phi} + \frac{k_{Brownain}}{k_f}\right) \frac{1}{\Theta_w - \Theta_M}\frac{\partial \Theta}{\partial Y}\bigg|_{Y=0} \tag{24}$$

$$Nu_r(X) = -\left(\frac{4}{3}Rd\right)\frac{1}{\Theta_w - \Theta_M}\frac{\partial \Theta}{\partial Y}\bigg|_{Y=0} \tag{25}$$

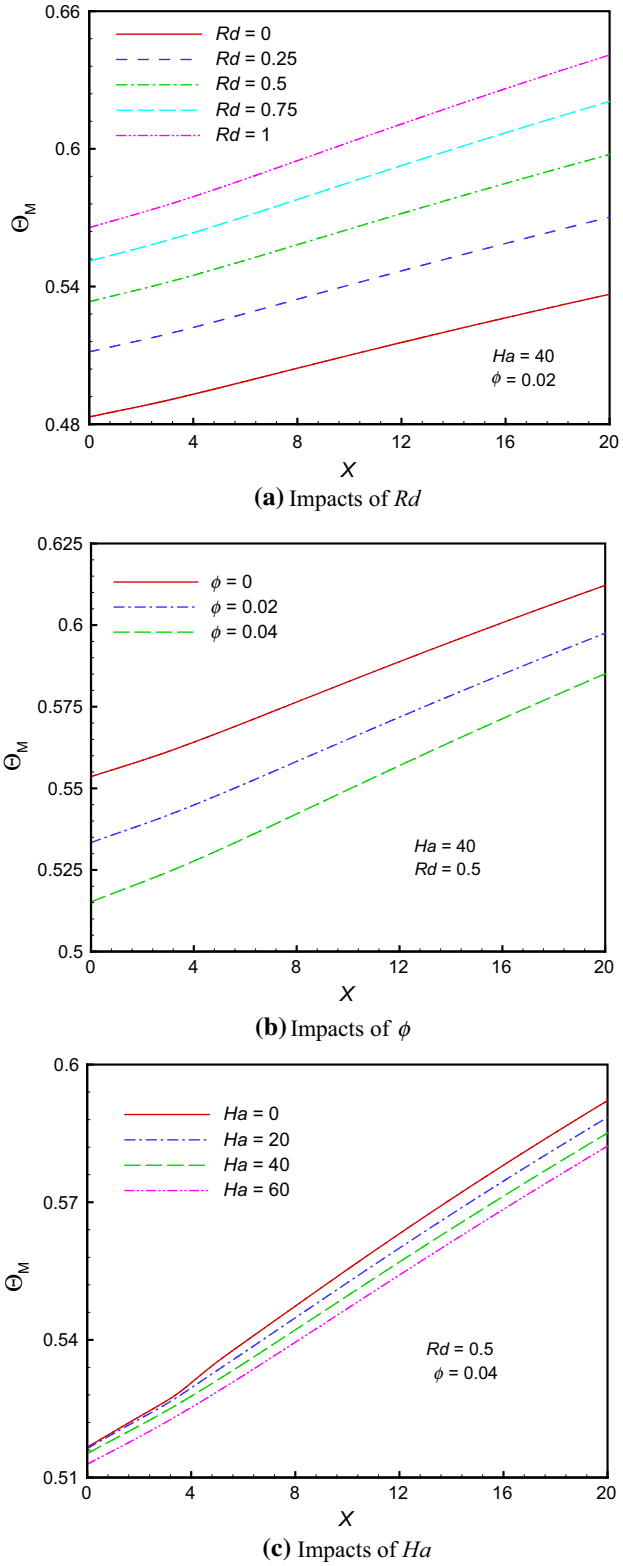


**Fig. 6** Impacts of different parameters on the $\Theta_M$ variations along the duct

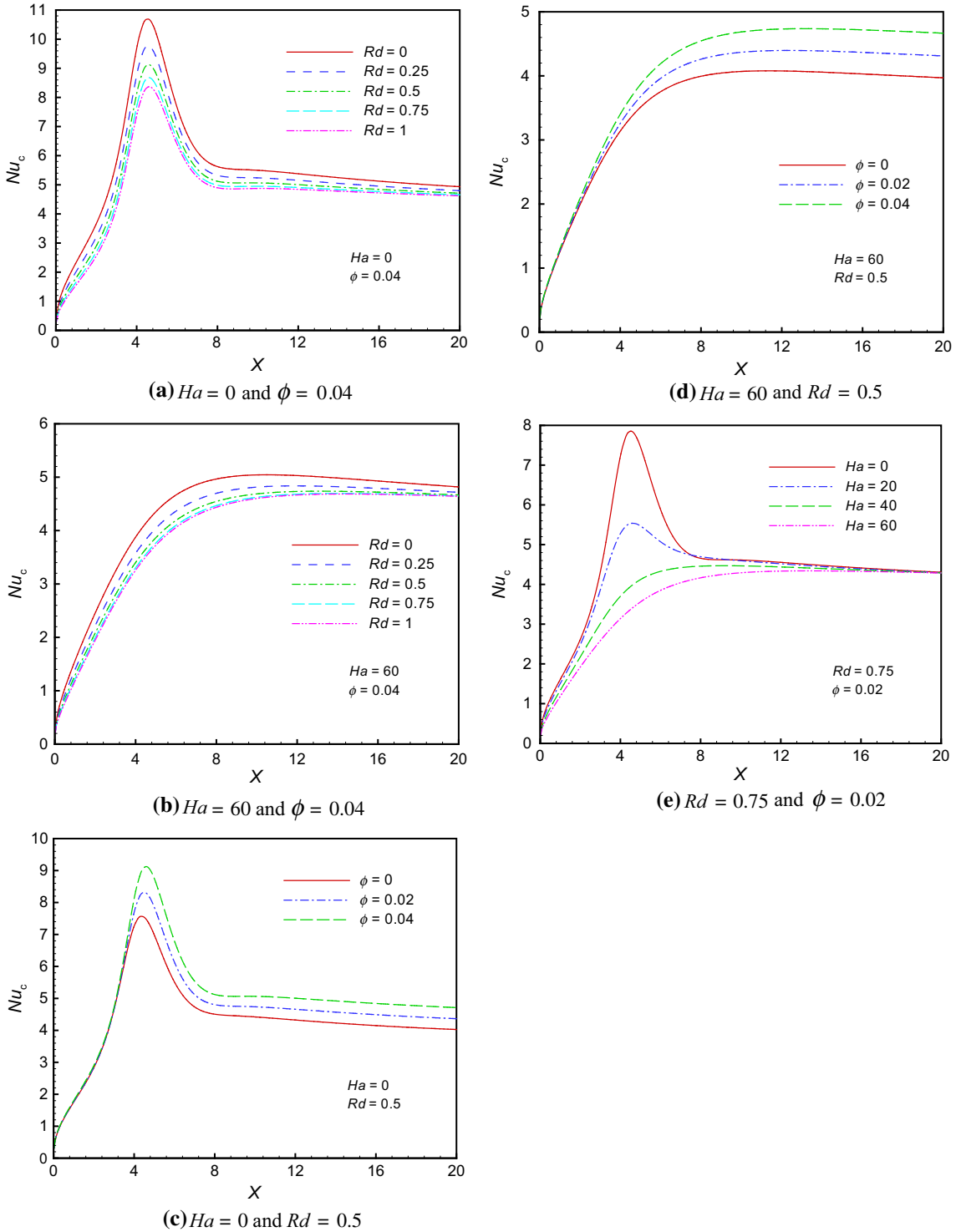


**Fig. 7** Variations of $Nu_c$ along the bottom wall at various magnitudes of $Rd, \phi$ and $Ha$ parameters

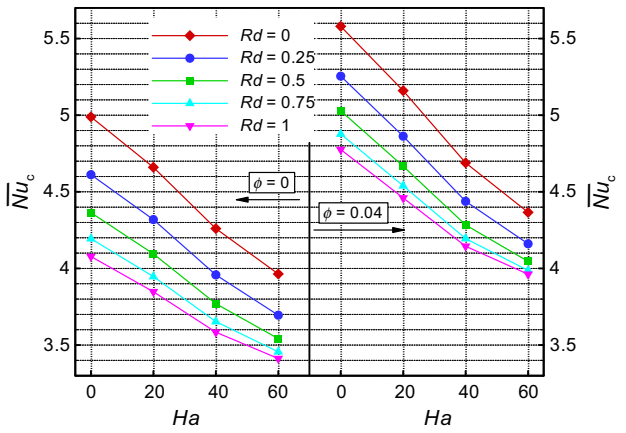


**Fig. 8** Impacts of the $Rd, \phi$ and $Ha$ parameters on the values of $\overline{Nu_c}$

$$Nu_t(X) = Nu_c(X) + Nu_r(X) = -\left(1 + \frac{3\left(\frac{k_s}{k_f} - 1\right)\phi}{\left(\frac{k_s}{k_f} + 2\right) - \left(\frac{k_s}{k_f} - 1\right)\phi} + \frac{k_{Brownain}}{k_f} + \frac{4}{3}Rd\right) \frac{1}{\Theta_w - \Theta_M}\frac{\partial \Theta}{\partial Y}\bigg|_{Y=0} \tag{26}$$

where the mean bulk temperature $(\Theta_M)$ is defined as:

$$\Theta_M(X) = \frac{\int_0^1 U\Theta dY}{\int_0^1 U dY} \tag{27}$$

## Numerical solution and validation results

The basic Eqs. (19)–(22) are first discretized using the finite volume method (FVM) and are converted to the set of algebraic equations. Also, the pressure field $(P)$ is coupled with velocity fields $(U, V)$ using the SIMPLE algorithm [77]. Then, the obtained algebraic equations are solved numerically by the line-by-line (LBL) method and using a FORTRAN code. The blocked-off method [78–80] is employed for modeling the inclined wall of BFS in Cartesian coordinates. The convergence criterion is defined so that the sum of absolute residuals of $U, V, P$ and $\Theta$ variables is less than $10^{-5}$. Additionally, the following criterion is also employed to ensure the convergence of solution:

$$\text{Max}\left|\frac{\Gamma^{\xi}(m,n) - \Gamma^{\xi-1}(m,n)}{\Gamma^{\xi}(m,n)}\right| \leq 10^{-6}$$

where the $\xi$ symbol denotes the iteration level and the $\Gamma$ term points to all variables of $U, V, P$ and $\Theta$. To ensure that the obtained results are not dependent on the gird size, the grid independence analysis is carried out. Accordingly, a grid size of $675 \times 42$ $(X \times Y)$ is selected as the best mesh. Of course, the mentioned mesh is clustered near the channel and step walls to achieve more accuracy.

The numerical solution presented in the current research is validated with the results of two different studies. First, the magnitudes of maximum Nusselt number $(Nu_{Max})$ along the bottom wall of a channel with BFS and its position $(X_{Max})$ are compared with the simulated results by Abu-Nada [59]. To reach this goal, all conditions of the problem of Ref. [59] are applied in the computer program written to analyze the problem of the current research. These comparisons are demonstrated in Fig. 2 for the various magnitudes of nanoparticles concentration and Reynolds numbers at $ER = 2$. Moreover, a close agreement is observed between the presented results of this study and Ref. [59]. To check the correctness of the simulation results of nanofluid flow in the presence of magnetic field, the second comparison is carried out based on the findings of Aminossadati et al. [81]. The magnitudes of average Nusselt number $(\overline{Nu})$ and maximum temperature $(\Theta_{Max})$ are compared at various values of $Ha(Ha = 0, 10, 20, 30, 40)$ in Table 3. According to this table, the maximum difference between the results is about 1.65%; therefore, the simulated results in this research are validated.

## Results and discussions

First, influences of CuO and $Al_2O_3$ nanoparticles on the magnitudes of average total Nusselt number $\left(\overline{Nu_t} = \int_0^{\frac{L_D}{H}} Nu_t(X)dX\right)$ are presented in Table 4 at five various values of radiation parameter. As it is seen from this table, the magnitudes of $\overline{Nu_t}$ are different for $Al_2O_3$–$H_2O$ and CuO–$H_2O$ nanofluids. By choosing the CuO–$H_2O$ nanofluid as the working fluid, a higher $\overline{Nu_t}$ is obtained. This means that the impact of CuO nanoparticles on the heating and cooling procedures is greater than influence of $Al_2O_3$ nanoparticles. Therefore, the CuO–$H_2O$ nanofluid is selected to analyze the thermal behaviors at different values of radiation parameter $(Rd)$, Hartmann number $(Ha)$ and nanoparticles concentration $(\phi)$.

To clarify the influence of radiation heat transfer on the thermal features of MHD CuO–$H_2O$ nanofluid, isotherms contours are presented in Fig. 3a–d at different magnitudes of $Rd, \phi$ and $Ha$ parameters. According to these figures, all three parameters have a significant impact on the isotherms contours inside the channel. To further show the details of these impacts, the dimensionless temperature distributions $(\Theta)$ along $Y$ axis are also plotted in Fig. 4a–e at different locations of $X(X = 1, 2, 5, 10)$. According to these figures,

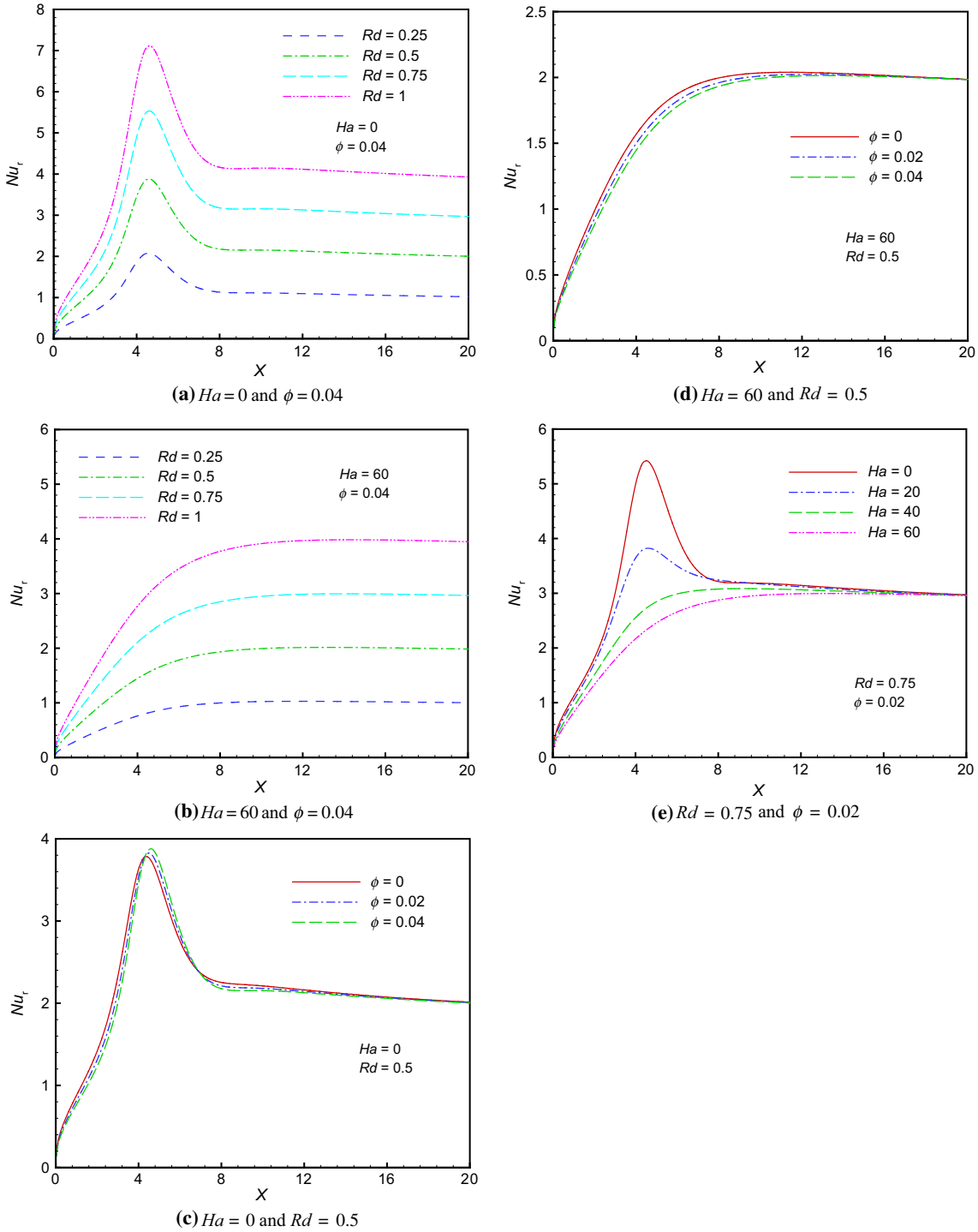


**Fig. 9** Variations of $Nu_r$ along the bottom wall at various magnitudes of $Rd, \phi$ and $Ha$ parameters

by augmentation of the radiation parameter, the $\Theta$ distribution becomes more homogeneous and approaches the temperature of the hot walls; such that the temperature gradients along the channel walls (especially along the bottom wall) reduce with increase in the $Rd$ parameter. Besides, any increase in the nanoparticles concentration results in a decrease in magnitudes of the $\Theta$ distribution. Of course, this reduction is negligible near the duct walls (especially near the bottom wall), so that the difference between the temperature gradients on these walls is very small. The impact of magnetic field on the $\Theta$ distribution is well seen from the gradients of temperature on the bottom

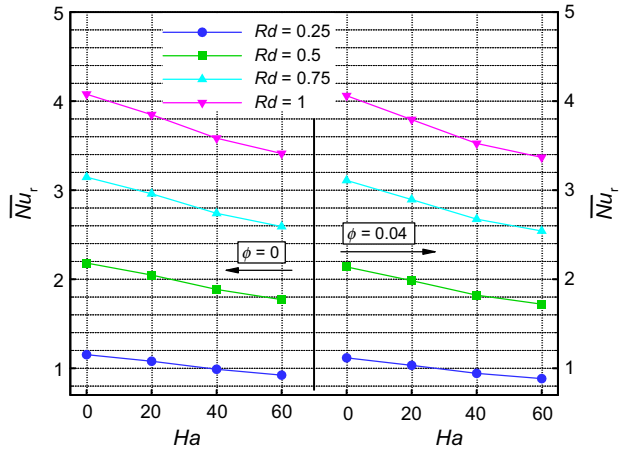


**Fig. 10** Impacts of the $Rd, \phi$ and $Ha$ parameters on the values of $\overline{Nu_r}$

wall $\left(\frac{\partial \Theta}{\partial Y}|_{Y=0}\right)$. In fact, the magnitudes of $\frac{\partial \Theta}{\partial Y}|_{Y=0}$ decrease by augmentation of $Ha$ number. Also, the role of recirculation zones on the $\Theta$ distribution is well illustrated in Figs. 3 and 4. To better understand this issue, the streamlines contours are shown in Fig. 5a and b at various magnitudes of $\phi$ and $Ha$ for $Rd = 0.5$. A significant recirculation zone (lower bubble) is created on the bottom wall downstream the BFS. The length of this region on the bottom wall $(L_r)$ enhances with augment of $\phi$ and $Ha$ parameters. Besides, the secondary recirculation region (upper bubble) is formed on the top wall in the absence of Lorentz force $(Ha = 0)$. The extent of this region increases by enhancing the $\phi$ parameter.

The main bulk temperature $(\Theta_M)$ is one of the important factors in determining the thermal characteristics. The impacts of $Rd, \phi$ and $Ha$ parameters on the variations of $\Theta_M$ along the duct are shown in Fig. 6a–c. In all cases, the $\Theta_M$ enhances along the channel in the axial direction of flow, due to both radiative and convective heat transfer mechanisms. However, the increase in $Rd$ parameter and consequently enhancement of thermal radiation heat transfer leads to an augmentation in the $\Theta_M$ magnitudes, while it decreases with increase in the $\phi$ and $Ha$ parameters.

Considering the significant effects of $Rd, \phi$ and $Ha$ parameters on the temperature distributions and mean bulk temperature; it is expected that the heat transfer rates are affected by these parameters. In the next figures, an attempt is performed to analyze this issue. Impacts of $Rd, \phi$ and $Ha$ parameters on the convective Nusselt number $(Nu_c)$ along the bottom $\left(0 \le X \le \frac{L_D}{H}, Y = 0\right)$ are displayed in Fig. 7a–e. As it is seen from these figures, both the trends and magnitudes of $Nu_c$ are dependent on the $Ha$ number, whereas the $Rd$ and $\phi$ parameters only affect its values. In fact, the difference between the trends of $Nu_c$ distributions at various magnitudes of $Ha$ is seen at the lower recirculation zone and near to the reattachment point $(X_r)$. In the case of $Ha = 0$, the $Nu_c$ has a local maximum value $(Nu_{c_{Max}})$ near the reattachment point, while the magnitude of $Nu_{c_{Max}}$ decreases with augmentation of $Ha$ number, such that the $Nu_c$ distribution lacks a peak in the highest value of $Ha$ number $(Ha = 60)$. However, the $Nu_c$ decreases with enhancing the radiation parameter and Hartmann number, but it enhances with increase in the concentration of CuO nanoparticles. These treatments can be also seen from the magnitudes of average convective Nusselt number $\left(\overline{Nu_c} = \int_0^{\frac{L_D}{H}} Nu_c(X)dX\right)$ against the various values of $Rd, \phi$ and $Ha$ parameters, which are reported in Fig. 8. Based on Fig. 8, the maximum rate of convective heat transfer occurs in the absence of thermal radiation and magnetic field and for the nanofluid with highest value of nanoparticles concentration $(Rd = 0, Ha = 0, \phi = 0.04)$. With respect to Eq. (24) and the presented explanations about the $\frac{\partial \Theta}{\partial Y}$ and $\Theta_M$, it can be concluded that the reduction of $Nu_c$ in terms of $Rd$ parameter is due to the decrease of $\frac{\partial \Theta}{\partial Y}|_{Y=0}$, whereas its enhancement against the $\phi$ parameter is related to the increase in $\frac{k_{nf}}{k_f}$ term. Also, the decrease of $\frac{\partial \Theta}{\partial Y}|_{Y=0}$ and $\Theta_M$ terms against $Ha$ number is the main reason for reducing the $Nu_c$ in terms of this number.

Influences of $Rd, \phi$ and $Ha$ parameters on the radiative Nusselt number $(Nu_r)$ distributions along the bottom wall are shown in Fig. 9a–e. Comparing the presented results in Figs. 7 and 9 clearly shows that trends of $Nu_r$ distribution are similar to the trends of $Nu_c$ distribution. Therefore, additional explanations are not presented to avoid repetition. According to Figs. 9 and 10, the $Nu_r$ and its average $\left(\overline{Nu_r} = \int_0^{\frac{L_D}{H}} Nu_r(X)dX\right)$ enhance significantly with augmentation of radiation parameter. This enhancement is due to an increase in the magnitude of $\Theta_M$ parameter and the direct presence of $Rd$ parameter in calculating the radiative Nusselt number. But, the $Nu_r$ and $\overline{Nu_r}$ reduce with the increase in the $Ha$ number because of the decrease of $\Theta_M$ and $\frac{\partial \Theta}{\partial Y}|_{Y=0}$ terms against this number. A noteworthy point in Fig. 9 is that the impact of $\phi$ parameter on the magnitudes of $Nu_r$ is dependent on the values of $Ha$ number. In the case of $Ha = 60$, this impact is generally decreasing, while in the absence of magnetic field $(Ha = 0)$, this influence is different in different zones. However, Fig. 10 clearly presents that the overall effect of concentration of nanoparticles on the $\overline{Nu_r}$ is small and decreasing. In fact, this reduction is due to a decrease in the values of $\Theta_M$ against the $\phi$ variable.

Originally, overall heat transfer characteristics of the thermal systems can be specified by calculating the total

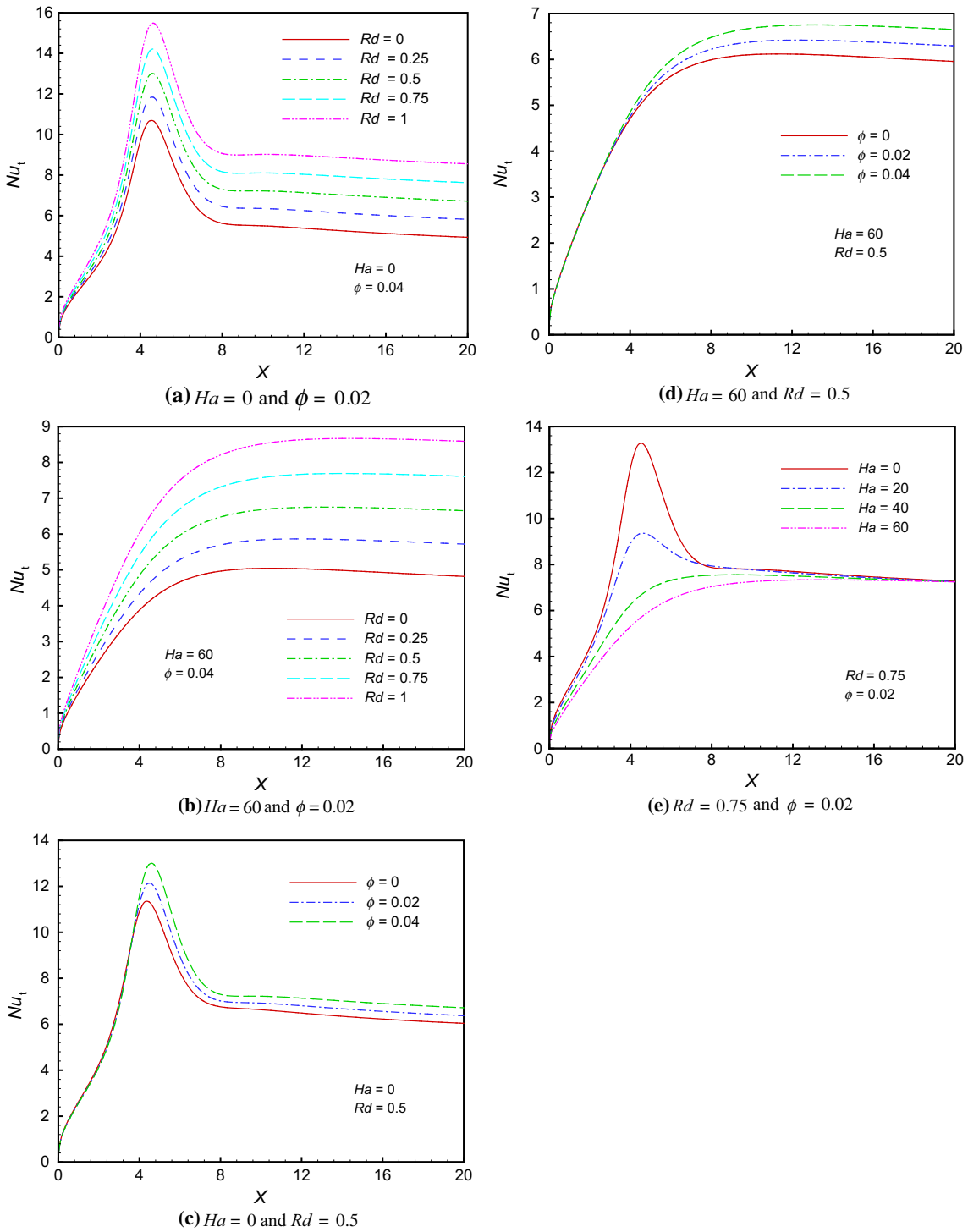


**Fig. 11** Variations of $Nu_t$ along the bottom wall at various magnitudes of $Rd, \phi$ and $Ha$ parameters

Nusselt number $(Nu_t)$. Distributions of $Nu_t$ along the bottom wall are displayed in Fig. 11a–e at various values of $Rd, \phi$ and $Ha$ parameters. These figures clearly show that the trends of $Nu_t$ distribution are similar to the variations of the $Nu_c$ and $Nu_r$. As it is shown in Fig. 11a–e, the $Nu_t$ enhances with augmentation of the $Rd$ and $\phi$ parameters, but it reduces with increase in the $Ha$ number. These results are also confirmed by calculating the magnitudes of average total Nusselt number $\left(\overline{Nu_t}\right)$ in Fig. 12. Based on this figure, the highest magnitude of total heat transfer rate occurs in the absence of Lorentz force and for the highest

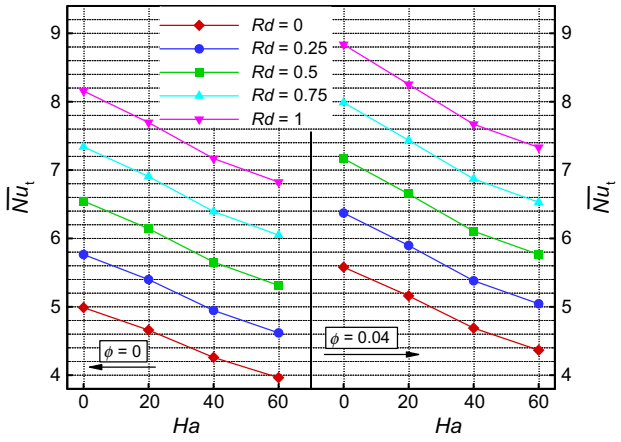


**Fig. 12** Impacts of the $Rd, \phi$ and $Ha$ parameters on the values of $\overline{Nu}_t$

values of radiation parameter and nanoparticles concentration $(Ha = 0, Rd = 1, \phi = 0.04)$.

## Conclusions

Interacting impacts of radiative heart transfer, Lorentz force and Brownian movement on the thermal features of MHD nanofluid flow over an inclined BFS are analyzed with details. The main results of this research can be summarized as follows:

- The CuO nanoparticles have a greater impact on heat transfer rates in comparison to the $Al_2O_3$ nanoparticles.
- The trends and magnitudes of $Nu_c$, $Nu_r$ and $Nu_t$ along the bottom wall are dependent on the $Ha$ number, while the $Rd$ and $\phi$ parameters only affect their values.
- An enhancement in the radiation parameter leads to an increase in the magnitudes of radiative and total heat transfer rates, while the values of convective heat transfer rate reduce with increase in this parameter. As for the case of $Ha = 20$ and $\phi = 0.04$, the $\overline{Nu_r}$ and $\overline{Nu_t}$ enhance about 261.92% and 39.96%, respectively, when the $Rd$ parameter rises from 0.25 to 1, while the reduction rate of the $\overline{Nu_c}$ is about 8.28%

$$\left(\left|\frac{\overline{Nu_t}\big|_{Rd=1} - \overline{Nu_t}\big|_{Rd=0.25}}{\overline{Nu_t}\big|_{Rd=0.25}}\right| \times 100 = 39.96\%\right).$$

- All heat transfer rates decrease with augmentation of the magnetic field strength, such that for the case of $Rd = 0.5$ and $\phi = 0.04$, the $\overline{Nu_c}$, $\overline{Nu_r}$ and $\overline{Nu_t}$ variables reduce, respectively, about 19.54%, 19.55% and 19.57% when the $Ha$ number changes from 0 to 60

$$\left(\left|\frac{\overline{Nu_t}\big|_{Ha=60} - \overline{Nu_t}\big|_{Ha=0}}{\overline{Nu_t}\big|_{Ha=0}}\right| \times 100 = 19.57\%\right).$$

- By adding the CuO nanoparticle to the water-based flow, convective and total heat transfer rates enhance. As for the case of $Rd = 0.5$ and $Ha = 20$, the $\overline{Nu_c}$ and $\overline{Nu_t}$ increase, respectively, about 13.96% and 8.27% when the nanoparticles concentration rises to 4%

$$\left(\left|\frac{\overline{Nu_t}\big|_{\phi=0.04} - \overline{Nu_t}\big|_{\phi=0}}{\overline{Nu_t}\big|_{\phi=0}}\right| \times 100 = 8.27\%\right).$$

Also, the impact of $\phi$ parameter on the $\overline{Nu_r}$ variable decreases about 3.07%.

## References

1. Bovand M, Rashidi S, Esfahani JA. Optimum interaction between magnetohydrodynamics and nanofluid for thermal and drag management. J Thermophys Heat Transf. 2016;31(1):218–29.
2. Rashidi MM, Nasiri M, Khezerloo M, Laraqi N. Numerical investigation of magnetic field effect on mixed convection heat transfer of nanofluid in a channel with sinusoidal walls. J Magn Magn Mater. 2016;401:159–68.
3. Sheikholeslami M, Rokni HB. Simulation of nanofluid heat transfer in presence of magnetic field: a review. Int J Heat Mass Transf. 2017;115:1203–33.
4. Öztop HF, Sakhrieh A, Abu-Nada E, Al-Salem K. Mixed convection of MHD flow in nanofluid filled and partially heated wavy walled lid-driven enclosure. Int Commun Heat Mass Transf. 2017;86:42–51.
5. Sheikholeslami M, Gerdroodbary MB, Mousavi SV, Ganji DD, Moradi R. Heat transfer enhancement of ferrofluid inside an 90° elbow channel by non-uniform magnetic field. J Magn Magn Mater. 2018;460:302–11.
6. Sajjadi H, Delouei AA, Atashafrooz M, Sheikholeslami M. Double MRT lattice Boltzmann simulation of 3-D MHD natural convection in a cubic cavity with sinusoidal temperature distribution utilizing nanofluid. Int J Heat Mass Transf. 2018;126:489–503.
7. Mehryan SAM, Izadi M, Namazian Z, Chamkha AJ. Natural convection of multi-walled carbon nanotube–$Fe_3O_4$/water magnetic hybrid nanofluid flowing in porous medium considering the impacts of magnetic field-dependent viscosity. J Therm Anal Calorim. 2019. https://doi.org/10.1007/s10973-019-08164-1.
8. Animasaun IL, Mahanthesh B, Jagun AO, Bankole TD, Sivaraj R, Shah NA, Saleem S. Significance of Lorentz force and thermoelectric on the flow of 29 nm CuO–water nanofluid on an upper horizontal surface of a paraboloid of revolution. J Heat Transf. 2019;141(2):022402.
9. Izadi M, Mohebbi R, Delouei AA, Sajjadi H. Natural convection of a magnetizable hybrid nanofluid inside a porous enclosure subjected to two variable magnetic fields. Int J Mech Sci. 2019;151:154–69.
10. Sajjadi H, Delouei AA, Izadi M, Mohebbi R. Investigation of MHD natural convection in a porous media by double MRT

lattice Boltzmann method utilizing MWCNT–$Fe_3O_4$/water hybrid nanofluid. Int J Heat Mass Transf. 2019;132:1087–104.
11. Sheikholeslami M. New computational approach for exergy and entropy analysis of nanofluid under the impact of Lorentz force through a porous media. Comput Methods Appl Mech Eng. 2019;344:319–33.
12. Sidik NAC, Mohammed HA, Alawi OA, Samion S. A review on preparation methods and challenges of nanofluids. Int Commun Heat Mass Transf. 2014;54:115–25.
13. Rashidi S, Bovand M, Esfahani JA, Ahmadi G. Discrete particle model for convective $Al_2O_3$–water nanofluid around a triangular obstacle. Appl Therm Eng. 2016;100:39–54.
14. Sidik NAC, Yazid MNAWM, Samion S, Musa MN, Mamat R. Latest development on computational approaches for nanofluid flow modeling: Navier–Stokes based multiphase models. Int Commun Heat Mass Transf. 2016;74:114–24.
15. Sheikholeslami M, Rokni HB. Free convection of CuO–$H_2O$ nanofluid in a curved porous enclosure using mesoscopic approach. Int J Hydrogen Energy. 2017;42(22):14942–9.
16. Maskaniyan M, Rashidi S, Esfahani JA. A two-way couple of Eulerian–Lagrangian model for particle transport with different sizes in an obstructed channel. Powder Technol. 2017;312:260–9.
17. Upadhyaa SM, Rajub CSK, Saleem S. Nonlinear unsteady convection on micro and nanofluids with Cattaneo–Christov heat flux. Results Phys. 2018;9:779–86.
18. Izadi M, Hashemi Pour SMR, Yasuri AK, Chamkha AJ. Mixed convection of a nanofluid in a three-dimensional channel. J Therm Anal Calorim. 2018. https://doi.org/10.1007/s10973-018-7889-0.
19. Nasiri H, Jamalabadi MYA, Sadeghi R, Safaei MR, Nguyen TK, Shadloo MS. A smoothed particle hydrodynamics approach for numerical simulation of nano-fluid flows. J Therm Anal Calorim. 2018. https://doi.org/10.1007/s10973-018-7022-4.
20. Afridi MI, Qasim M, Saleem S. Second law analysis of three dimensional dissipative flow of hybrid nanofluid. J Nanofluids. 2018;7(6):1272–80.
21. Nakhchi ME, Esfahani JA. Cu–water nanofluid flow and heat transfer in a heat exchanger tube equipped with cross-cut twisted tape. Powder Technol. 2018;339:985–94.
22. Akbarzadeh M, Rashidi S, Karimi N, Omar N. First and second laws of thermodynamics analysis of nanofluid flow inside a heat exchanger duct with wavy walls and a porous insert. J Therm Anal Calorim. 2019;135(1):177–94.
23. Nakhchi ME, Esfahani JA. Numerical investigation of turbulent Cu–water nanofluid in heat exchanger tube equipped with perforated conical rings. Adv Powder Technol. 2019;30(7):1338–47.
24. Rashidi S, Javadi P, Esfahani JA. Second law of thermodynamics analysis for nanofluid turbulent flow inside a solar heater with the ribbed absorber plate. J Therm Anal Calorim. 2019;135(1):551–63.
25. Rashidi S, Eskandarian M, Mahian O, Poncet S. Combination of nanofluid and inserts for heat transfer enhancement. J Therm Anal Calorim. 2019;135(1):437–60.
26. Nakhchi ME, Esfahani JA. Entropy generation of turbulent Cu–water nanofluid flow in a heat exchanger tube fitted with perforated conical rings. J Therm Anal Calorim. 2019. https://doi.org/10.1007/s10973-019-08169-w.
27. Oztop HF, Al-Salem K, Pop I. MHD mixed convection in a lid-driven cavity with corner heater. Int J Heat Mass Transf. 2011;54:3494–504.
28. Shirvan KM, Mamourian M, Mirzakhanlari S, Moghiman M. Investigation on effect of magnetic field on mixed convection heat transfer in a ventilated square cavity. Proc Eng. 2015;127:1181–8.
29. Sajjadi H, Kefayati GR. MHD turbulent and laminar natural convection in a square cavity utilizing lattice Boltzmann method. Heat Transf Asian Res. 2016;45(8):795–814.
30. Rashidi S, Esfahani JA, Maskaniyan M. Applications of magnetohydrodynamics in biological systems-a review on the numerical studies. J Magn Magn Mater. 2017;439:358–72.
31. Babu MJ, Sandeep N, Saleem S. Free convective MHD Cattaneo-Christov flow over three different geometries with thermophoresis and Brownian motion. Alex Eng J. 2017;56(4):659–69.
32. Kumar MS, Sandeep N, Kumar BR, Saleem S. Effect of aligned magnetic field on MHD squeezing flow of Casson fluid between parallel plates. Defect Diffus Forum. 2018;384:1–11.
33. Sajjadi H, Delouei AA, Sheikholeslami M, Atashafrooz M, Succi S. Simulation of three dimensional MHD natural convection using double MRT lattice Boltzmann method. Phys A. 2019;515:474–96.
34. Sheikholeslami M, Ganji DD, Javed MY, Ellahi R. Effect of thermal radiation on magnetohydrodynamics nanofluid flow and heat transfer by means of two phase model. J Magn Magn Mater. 2015;374:36–43.
35. Shehzad SA, Hayat T, Alsaedi A, Ahmad B. Effects of thermophoresis and thermal radiation in mixed convection three-dimensional flow of Jeffrey fluid. Appl Math Mech. 2015;36(5):655–68.
36. Hussain T, Hayat T, Shehzad SA, Alsaedi A, Chen B. A model of solar radiation and joule heating in flow of third grade nanofluid. Zeitschrift für Naturforschung A. 2015;70(3):177–84.
37. Shehzad SA, Abdullah Z, Alsaedi A, Abbasi FM, Hayat T. Thermally radiative three-dimensional flow of Jeffrey nanofluid with internal heat generation and magnetic field. J Magn Magn Mater. 2016;397:108–14.
38. Sheikholeslami M, Shehzad SA. Thermal radiation of ferrofluid in existence of Lorentz forces considering variable viscosity. Int J Heat Mass Transf. 2017;109:82–92.
39. Sheikholeslami M. Magnetic field influence on nanofluid thermal radiation in a cavity with tilted elliptic inner cylinder. J Mol Liq. 2017;229:137–47.
40. Rashid M, Khan MI, Hayat T, Khan MI, Alsaedi A. Entropy generation in flow of ferromagnetic liquid with nonlinear radiation and slip condition. J Mol Liq. 2019;276:441–52.
41. Ghalambaz M, Sabour M, Pop I. Free convection in a square cavity filled by a porous medium saturated by a nanofluid: viscous dissipation and radiation effects. Eng Sci Technol Int J. 2016;19(3):1244–53.
42. Sheikholeslami M, Hayat T, Alsaedi A. MHD free convection of $Al_2O_3$–water nanofluid considering thermal radiation: a numerical study. Int J Heat Mass Transf. 2016;96:513–24.
43. Safaei MR, Karimipour A, Abdollahi A, Nguyen TK. The investigation of thermal radiation and free convection heat transfer mechanisms of nanofluid inside a shallow cavity by lattice Boltzmann method. Phys A. 2018;509:515–35.
44. Sheikholeslami M, Sajjadi H, Delouei AA, Atashafrooz M, Li Z. Magnetic force and radiation influences on nanofluid transportation through a permeable media considering $Al_2O_3$ nanoparticles. J Therm Anal Calorim. 2019;136(6):2477–85.
45. Sheikholeslami M, Rokni HB. Numerical simulation for impact of Coulomb force on nanofluid heat transfer in a porous enclosure in presence of thermal radiation. Int J Heat Mass Transf. 2018;118:823–31.
46. Feng YY, Wang CH. Discontinuous finite element method with a local numerical flux scheme for radiative transfer with strong inhomogeneity. Int J Heat Mass Transf. 2018;126:783–95.
47. Wang CH, Feng YY, Yue K, Zhang XX. Discontinuous finite element method for combined radiation-conduction heat transfer in participating media. Int Commun Heat Mass Transf. 2019;108,

104287. https://doi.org/10.1016/j.icheatmasstransfer.2019.104287.
48. Nouri-Borujerdi A, Nakhchi ME. Experimental study of convective heat transfer in the entrance region of an annulus with an external grooved surface. Exp Thermal Fluid Sci. 2018;98:557–62.
49. Nakhchi ME. Experimental optimization of geometrical parameters on heat transfer and pressure drop inside sinusoidal wavy channels. Thermal Sci Eng Prog. 2019;9:121–31.
50. Nouri-Borujerdi A, Nakhchi ME. Friction factor and Nusselt number in annular flows with smooth and slotted surface. Heat Mass Transf. 2019;55(3):645–53.
51. Oztop HF, Mushatet KS, Yılmaz İ. Analysis of turbulent flow and heat transfer over a double forward facing step with obstacles. Int Commun Heat Mass Transf. 2012;39(9):1395–403.
52. Atashafrooz M, Gandjalikhan Nassab SA. Simulation of laminar mixed convection recess flow combined with radiation heat transfer. Iran J Sci Technol Trans Mech Eng. 2013;37(M1):71–5.
53. Selimefendigil F, Oztop HF. Numerical analysis of laminar pulsating flow at a backward facing step with an upper wall mounted adiabatic thin fin. Comput Fluids. 2013;88:93–107.
54. Atashafrooz M, Nassab SAG, Lari K. Application of full-spectrum k-distribution method to combined non-gray radiation and forced convection flow in a duct with an expansion. J Mech Sci Technol. 2015;29(2):845–59.
55. Atashafrooz M, Gandjalikhan Nassab SA, Lari K. Numerical analysis of interaction between non-gray radiation and forced convection flow over a recess using the full-spectrum k-distribution method. Heat Mass Transf. 2016;52(2):361–77.
56. Kherbeet AS, Safaei MR, Mohammed HA, Salman BH, Ahmed HE, Alawi OA, Al-Asadi MT. Heat transfer and fluid flow over microscale backward and forward facing step: a review. Int Commun Heat Mass Transf. 2016;76:237–44.
57. Atashafrooz M, Gandjalikhan Nassab SA, Lari K. Coupled thermal radiation and mixed convection step flow of non-gray gas. J Heat Transf (ASME). 2016;138(7):072701–9.
58. Nouri-Borujerdi A, Moazezi A. Investigation of obstacle effect to improve conjugate heat transfer in backward facing step channel using fast simulation of incompressible flow. Heat Mass Transf. 2018;54(1):135–50.
59. Abu-Nada E. Application of nanofluids for heat transfer enhancement of separated flows encountered in a backward facing step. Int J Heat Fluid Flow. 2008;29:242–9.
60. Al-aswadi AA, Mohammed HA, Shuaib NH, Campo A. Laminar forced convection flow over a backward facing step using nanofluids. Int Commun Heat Mass Transf. 2010;37(8):950–7.
61. Mohammed HA, Golieskardi M, Munisamy KM, Wahid MA. Combined convection heat transfer of nanofluids flow over forward facing step in a channel having a blockage. Appl Mech Mater. 2013;388:185–91.
62. Safaei MR, Togun H, Vafai K, Kazi SN, Badarudin A. Investigation of heat transfer enhancement in a forward-facing contracting channel using FMWCNT nanofluids. Numer Heat Transf A: Appl. 2014;66(12):1321–40.
63. Togun H, Safaei MR, Sadri R, Kazi SN, Badarudin A, Hooman K, Sadeghinezhad E. Numerical simulation of laminar to turbulent nanofluid flow and heat transfer over a backward-facing step. Appl Math Comput. 2014;239:153–70.
64. Mohammed HA, Alawi OA, Wahid MA. Mixed convective nanofluid flow in a channel having backward-facing step with a baffle. Powder Technol. 2015;275:329–43.
65. Mohammed HA, Al-aswadi AA, Abu-Mulaweh HI, Shuaib NH. Influence of nanofluids on mixed convective heat transfer over a horizontal backward facing step. Heat Transf Asian Res. 2011;40(4):287–307.
66. Alawi OA, Sidik NAC, Kazi SN, Abdolbaqi MK. Comparative study on heat transfer enhancement and nanofluids flow over backward and forward facing steps. J Adv Res Fluid Mech Thermal Sci. 2016;23(1):25–49.
67. Selimefendigil F, Oztop HF. Numerical study of forced convection of nanofluid flow over a backward facing step with a corrugated bottom wall in the presence of different shaped obstacles. Heat Transf Eng. 2016;37(15):1280–92.
68. Kherbeet AS, Mohammed HA, Salman BH, Ahmed HE, Alawi OA, Rashidi MM. Experimental study of nanofluid flow and heat transfer over microscale backward- and forward-facing steps. Exp Thermal Fluid Sci. 2015;65:13–21.
69. Kherbeet AS, Mohammed HA, Ahmed HE, Salman BH, Alawi OA, Safaei MR, Khazaal MT. Mixed convection nanofluid flow over microscale forward-facing step: effect of inclination and step heights. Int Commun Heat Mass Transf. 2016;78:145–54.
70. Atashafrooz M. Effects of Ag–water nanofluid on hydrodynamics and thermal behaviors of three-dimensional separated step flow. Alex Eng J. 2018;57:4277–85.
71. Abbassi H, Nassrallah SB. MHD flow and heat transfer in a backward-facing step. Int Commun Heat Mass Transf. 2007;34(2):231–7.
72. Selimefendigil F, Öztop HF. Influence of inclination angle of magnetic field on mixed convection of nanofluid flow over a backward facing step and entropy generation. Adv Powder Technol. 2015;26(6):1663–75.
73. Atashafrooz M, Sheikholeslami M, Sajjadi H, Delouei AA. Interaction effects of an inclined magnetic field and nanofluid on forced convection heat transfer and flow irreversibility in a duct with an abrupt contraction. J Magn Magn Mater. 2019;478:216–26.
74. Atashafrooz M. The effects of buoyancy force on mixed convection heat transfer of MHD nanofluid flow and entropy generation in an inclined duct with separation considering Brownian motion effects. J Therm Anal Calorim. 2019. https://doi.org/10.1007/s10973-019-08363-w.
75. Sheikholeslami M, Abelman S, Ganji DD. Numerical simulation of MHD nanofluid flow and heat transfer considering viscous dissipation. Int J Heat Mass Transf. 2014;79:212–22.
76. Sheikholeslami M, Ganji DD. Nanofluid flow and heat transfer between parallel plates considering Brownian motion using DTM. Comput Methods Appl Mech Eng. 2015;283:651–63.
77. Patankar SV, Spalding DB. A calculation procedure for heat, mass and momentum transfer in three-dimensional parabolic flows. Int J Heat Mass Transf. 1972;15(10):1787–806.
78. Atashafrooz M, Gandjalikhan Nassab SA. Simulation of three-dimensional laminar forced convection flow of a radiating gas over an inclined backward-facing step in a duct under bleeding condition. Inst Mech Eng C, J Mech Eng Sci. 2012;227(2):332–45.
79. Atashafrooz M, Gandjalikhan Nassab SA. Numerical analysis of laminar forced convection recess flow with two inclined steps considering gas radiation effect. Comput Fluids. 2012;66:167–76.
80. Atashafrooz M, Gandjalikhan Nassab SA. Combined heat transfer of radiation and forced convection flow of participating gases in a three-dimensional recess. J Mech Sci Technol. 2012;26(10):3357–68.
81. Aminossadati SM, Raisi A, Ghasemi B. Effects of magnetic field on nanofluid forced convection in a partially heated microchannel. Int J Non-Linear Mech. 2011;46:1373–82.